ELSEVIER

Bone 35 (2004) 11–20

BONE

www.elsevier.com/locate/bone

SEM and TEM study of the hierarchical structure of C57BL/6J and C3H/HeJ mice trabecular bone

Matthew A. Rubin,[a] Janet Rubin,[b] and Iwona Jasiuk[a,*]

[a] The G.W.W. School of Mechanical Engineering, Georgia Institute of Technology, Atlanta, GA 30332-0405, USA
[b] Emory University School of Medicine, Veterans Affairs Medicine Center, Decatur, GA 30033, USA

Received 10 October 2003; revised 17 January 2004; accepted 6 February 2004

Abstract

Transmission electron microscopy (TEM) and scanning electron microscopy (SEM) were used to study the hierarchical structure of trabecular bone from C57BL/6J (low bone mass) and C3H/HeJ mice (high bone mass). Bone was harvested from two different anatomical locations: femoral metaphysis and L5 vertebra. This investigation focused on three structural scales: the mesostructural (porous network of trabecular struts), the microstructural (collagen fibril arrangements in trabecular packets), and the nanostructural (collagen fibril and apatite crystals) levels. At the mesostructural level, no distinct differences were found in the trabecular structure of femoral metaphysis but thinner trabecular struts were observed in L5 vertebra for C57BL/6J mice strain. At the microstructural level, the collagen fibrils forming the rotated, twisted, and orthogonal plywood arrangements were distinguished as well as atypical arrangements. At the nanostructural level, the shape and size of apatite crystals, and their arrangement with respect to collagen fibrils were studied. In spite of very different bone mass densities, both mice strains had similar structures at the nanostructural and microstructural levels.

Keywords: C3H/HeJ and C57/6J mice; Trabecular bone; Bone hierarchical structure; Scanning electron microscopy; Transmission electron microscopy

Introduction

The risk of developing osteoporosis and excessive bone fragility in humans is in large part determined by the amount of bone mass accumulated during the active growth phases of early life and the subsequent rate of bone loss with aging [1,2]. Studies on human subjects have shown that 50–80%, depending on location, of the variability in peak bone density is genetically based, making it essential to understand the contribution of genetic factors to peak bone mass [3–8]. This makes studies of bone structure and morphology in humans difficult since the genetic background in humans varies significantly between each person. Inbred mice, in contrast, make very good models for evaluating the involvement of genetic factors in the determination of a given phenotype because they possess known genetic backgrounds [9–11]. The C3H/HeJ (C3H) and C57BL/6J (B6) inbred mice strains, which have the same weight and body size but are characterized high and low bone mass, respectively [9,11–23], are good candidates for such studies.

Bone has a hierarchical structure. In this paper, we distinguish the following structural levels: *mesostructural* (trabecular network in trabecular bone or collection of osteons in cortical bone), *microstructural* (lamellar arrangements of collagen fibrils), and *nanostructural* (collagen fibril and apatite crystal) levels.

The mesostructure of C3H and B6 bone has been investigated using histomorphometric measurements, peripheral quantitative computed tomography (pQCT), and microcomputed tomography (μCT). Histomorphometric measurements revealed that femoral and tibia cortical bone areas are significantly larger in C3H mice [9,24], and furthermore, the higher bone mineral density (BMD) in C3H mice is associated with greater trabecular (cancellous) bone volume and cortical bone area [25]. pQCT techniques also showed that C3H mice have higher femoral and vertebral volumetric bone mineral density (vBMD) compared to B6 mice [11,13,14]. Amblard et al.'s [26] assessment using μCT suggested that the higher femoral trabecular bone volume in C3H mice was due to thicker

* Corresponding author. The G.W.W. School of Mechanical Engineering, Georgia Institute of Technology, 801 Ferst Drive NW, Atlanta, GA 30332-0405. Fax: +1-404-894-0186.

E-mail addresses: mrubin77@yahoo.com (M.A. Rubin), jrubi02@emory.edu (J. Rubin), iwona.jasiuk@me.gatech.edu (I. Jasiuk).

8756-3282/$ - see front matter © 2004 Elsevier Inc. All rights reserved.
doi:10.1016/j.bone.2004.02.008

and more connected trabeculae, despite a comparable number of trabeculae in both mice strains. Conversely, Turner et al.'s [10,11] μCT studies concluded that C3H mice have reduced trabecular structure in proximal femur and lumbar vertebra compared to B6 mice. This discrepancy has not been resolved—further, differences in the bone structure of C3H and B6 mice at three hierarchical levels, mesostructural, microstructural, and nanostructural, have not been previously considered in detail.

Scanning electron microscopy (SEM) can help to resolve differences that may exist between the trabecular structure of C3H and B6 mice at the mesostructural level [27,28]. Additionally, transmission electron microscopy (TEM) can identify structural features at lower scales such as lamellar level (microstructural level) and fibril/crystal level (nanostructural level). TEM has been used to investigate the lamellar structure of bone, but its forte is the ability to image collagen fibrils and apatite crystals at the nanostructural level [29,30].

In the present hierarchical investigation, SEM and TEM are employed to characterize and identify structural differences in trabecular bone of B6 and C3H mice from the mesoscale down to the nanoscale. Also, SEM and TEM are used for the first time to analyze hierarchical structures of these two mice strains.

Materials and methods

Electron microscopy methods

A JEOL JEM-1210 Analytical TEM operated at 90 kV was used to view the calcified and decalcified mouse trabecular bone sections at the Integrated Microscopy and Microanalytical Facility at Emory University (Dr. Robert Apkarian, director). The focus was on the collagen fibril arrangement (lamellar structure) at the microstructural level and the collagen fibril/apatite crystal organization at the nanostructural level in C3H and B6 mice bone. To view the lamellar structure more clearly and expose the collagen framework, some bone samples were decalcified, that is, bone mineral was removed. The remaining bone samples stayed calcified and they were used to investigate the apatite crystal shape, size, and arrangement with respect to collagen fibrils. They were also compared with the lamellar structures in demineralized specimens. TEM images were photographed at low (2000×), intermediate (20,000×), and high magnifications (80,000×) (low-dose imaging) to best observe nanostructural features of bone. The negatives were then scanned with an Agfa T-2500 scanner into a computer to generate high-resolution, 45-MB image files. These images provided monitor magnification 10-fold greater than the recorded magnification for detail recognition. Adobe Photoshop 6.0 was then used to adjust the black, white, and gray tonal ranges of the images for better visualization and detail recognition of the bone crystals. An unpaired two-sample *t* test was used to analyze the statistical significance of crystal dimensions in C3H and B6 mice.

An ISI DS-130 LaB6 SEM operated at 9–10 kV was employed to investigate the trabecular architecture (mesostructural level) of the C3H and B6 mouse bone. The decalcification was not necessary for analyzing these structures under SEM, thus they all remained calcified. SEM images were digitally photographed at low (15×), intermediate (1000×), and high magnifications (10,000×) to best capture the trabecular structure. Images were then processed and analyzed using Adobe Photoshop 6.0.

Materials preparation

Inbred, 15- to 16-week-old C3H and B6 female mice (n = 8/breed) were obtained from Charles River Laboratories (from retired breeders). The Georgia Tech Institutional Animal Care and Use Committee (IACUC) approved all procedures involving animals. The left and right femurs (n = 32) as well as the L5 vertebra (n = 16) were excised from each mouse strain. Muscle and other adherent tissues were removed carefully with the use of surgical blades and forceps. All left femurs (n = 16) were placed in individual specimen containers filled with 2.5% paraformaldehyde in 0.1 M sodium phosphate buffer (pH 7.4) and stored at 4°C for 48 h. These samples were then submerged and stored at 4°C in the 0.1 M sodium phosphate buffer. Immediately after dissection, the right femoral metaphyses (n = 16) were sectioned transversely to the cortical shaft below lesser trochanter. Then, the proximal part was cut again in cross section, transversely to the cortical shaft, between greater and lesser trochanter. The proximal (upper) part of each cut femur, including a head and a greater trochanter, was prepared for SEM while the distal (lower) one with lesser trochanter was used for TEM. This sectioning was chosen to ensure that sections studied via SEM and TEM had a sufficient amount of trabecular bone for analysis. Only right femurs were used in the present study. (Note: There was no specific reason for choosing the proximal region over the distal region of the femur for TEM.) L5 vertebrae (n = 16) were also cut in cross section (transversely) roughly in two halves; the upper half was prepared for TEM while the lower half underwent preparation for SEM. Samples used for TEM were fixed with 2.5% paraformaldehyde in 0.1 M sodium phosphate buffer (pH 7.4) for 48 h and then stored in a 0.1-M sodium phosphate buffer. Samples used for SEM were placed in a 3% hydrogen peroxide solution.

Transmission electron microscopy preparation

Ten L5 mouse vertebrae (n = 5/C3H, n = 5/B6) and ten mouse femurs (n = 5/C3H, n = 5/B6) underwent standard chemical fixation and preparation for TEM. Additionally, six L5 mouse vertebrae (n = 3/C3H, n = 3/B6) and six

mouse femurs (n = 3/C3H, n = 3/B6) were decalcified for TEM.

Calcified bone

Mouse bone (n = 20) specimens were postfixed in 1% osmium tetroxide, dehydrated in an acetone series (30%, 50%, 70%, 80%, 90%, 100%), then infiltrated with a graded series of acetone and three changes of Spurr resin, and finally, embedded in fresh Spurr resin in labeled Beem™ capsules. Ultrathin sections (90–100 nm) of bone were then cut with a diamond knife on a RMC MT 7000 Ultramicrotome and picked up on 300-mesh copper and Formvar™-coated, single slot, copper grids. From each specimen, up to four blocks were selected for thin sections. From each block, several thin sections were cut and collected onto three copper grids. Concurrently, thick sections were also cut. These were used for viewing on light microscope to determine the orientation of bone in thin TEM sections.

Decalcification of bone samples

Mouse bone (n = 12) specimens were decalcified in 0.5 M EDTA, pH 8.0 (Tris), and 0.01% Sodium Azide solution at room temperature for 4 days. The EDTA was replaced with fresh solution every 24 h for 4 days. After 4 days, the specimens were rinsed and then submerged in an isotonic saline solution for 24 h at 4°C. The samples were then postfixed in 1% osmium tetroxide and the remaining procedures were the same as for calcified bone (see previous section).

Scanning electron microscopy preparation

To completely remove adherent tissue, bone samples were first immersed in a 3% hydrogen peroxide solution for 48 h at room temperature and then rinsed with distilled water. They were then defatted in a solution of 50:50 methanol/chloroform for 24 h at room temperature. Samples were then put in a 5% Trypsin solution (pH 7.4) at room

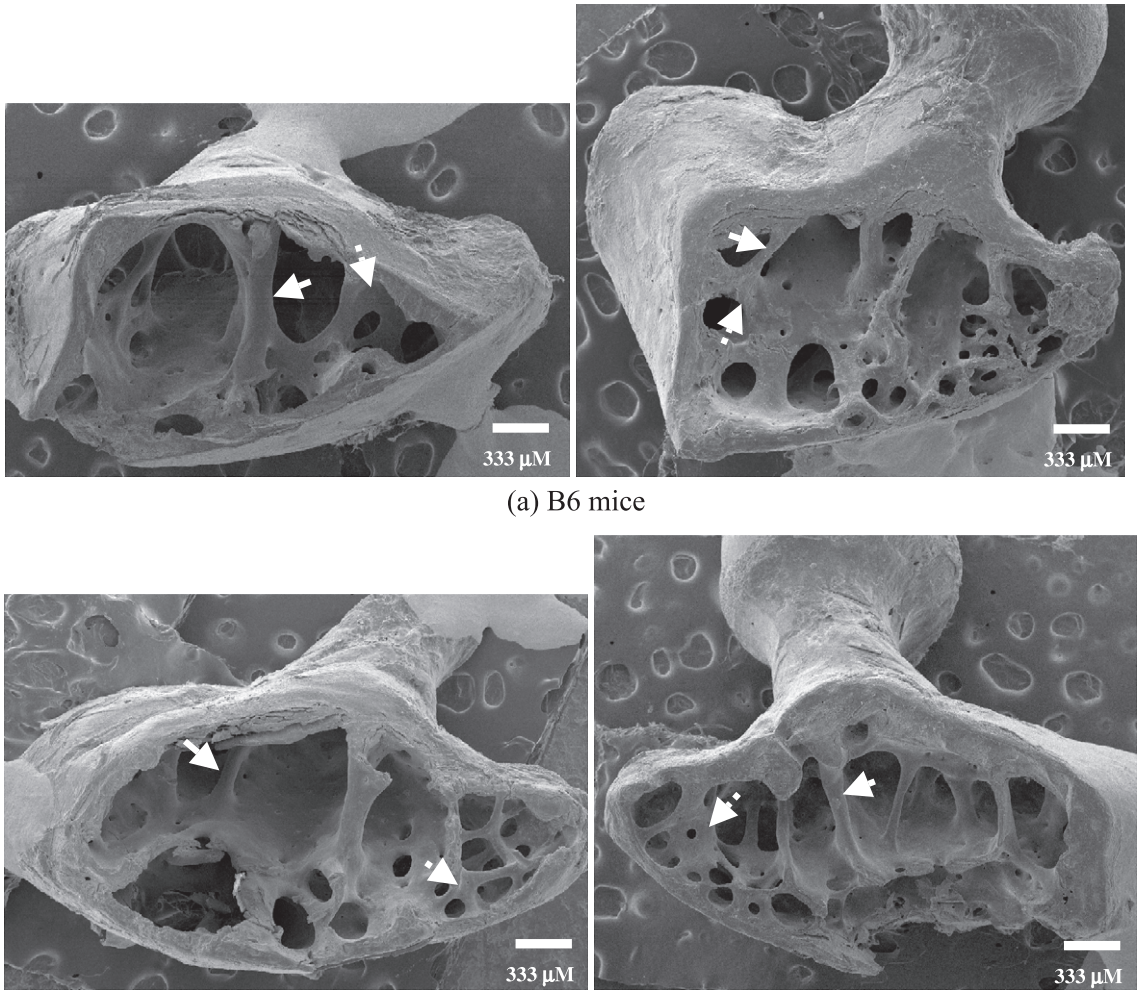

Fig. 1. SEM micrographs of the femoral metaphyseal region in (a) B6 mice and (b) C3H mice. Dotted arrows denote plate-like trabecula; solid arrows denote rod-like trabecula.

temperature for 48 h to remove any remaining adherent tissue. The specimens were further rinsed with distilled water until examination under a dissection microscope revealed no soft tissue on the bone. When no observable soft tissue remained, the specimens were placed in a desiccator to dry out. The desiccator was vented every 24 h to release any moisture or fumes emitted from the bone. As soon as the samples were dry, they were coated with 60:40 gold-Palladium by sputtering with a SC500 emscope.

Measurement of crystals dimensions

To measure crystal dimensions, we focused on the mineral regions of mineralized bone in TEM images where crystal profiles of plate-like and tablet-like shapes were observed. However, due to the overlapping of crystal profiles, it was not possible to measure the lengths and widths of crystals. The thickness of the crystals, on the other hand, was readily discernable and was generally uniform throughout the micrographs. Crystals that had well-defined profiles were measured carefully on each image. Twenty-two crystals were measured for each mice strain (n = 22). Crystals that were in clusters were not used in measurements. For more details on the measurement procedure, see Rubin et al. [33].

Results

Mesostructure

SEM micrographs revealed little structural difference in the trabecular architecture in the metaphyseal regions of the femur of B6 mouse (Fig. 1a) and C3H mouse bone

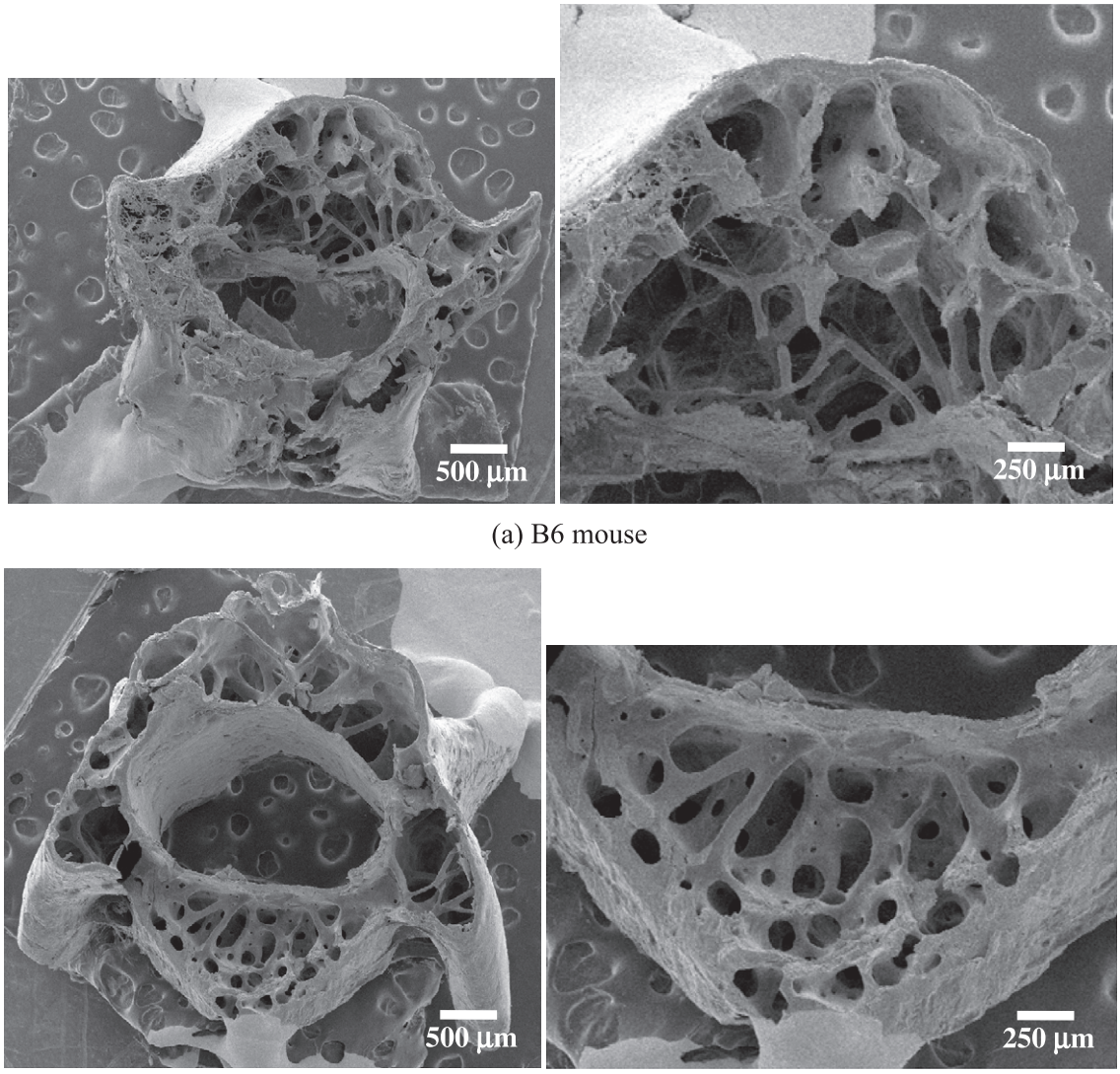

Fig. 2. SEM micrograph of a L5 vertebra from (a) B6 mouse and (b) C3H mouse (left). Close-up of the trabecular microstructure (right).

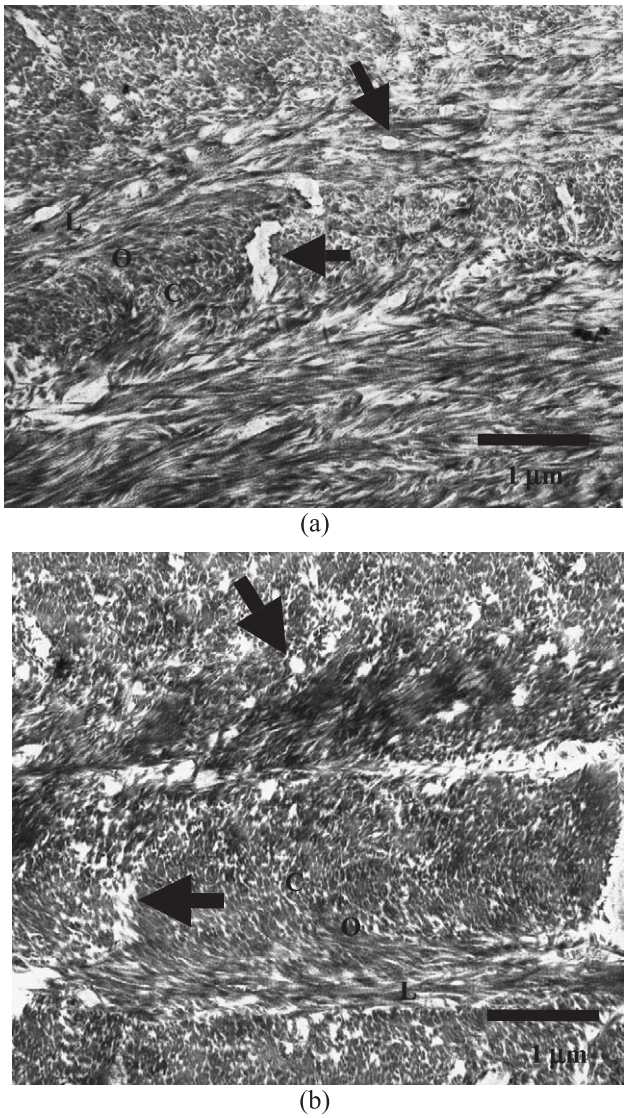

Fig. 3. TEM micrograph of the characteristic arcing pattern of a demineralized twisted or rotated plywood motif in (a) B6 mouse and (b) C3H mouse. A successive transition of longitudinal (L), oblique (O), and cross-sectioned fibrils (C) is apparent. Canaliculi (arrows), which appear as white elliptical bodies with variable length and size, are positioned in or traversing the lamellar structure.

(Fig. 1b). The central metaphyseal region in both mice strains showed sparse trabecular structure consisting of thick, long, rod-like trabecula that spanned from the metaphyseal cortex until they were intersected by flat, plate-like sheets of bone. These rod-like trabeculae had a fairly uniform diameter and possessed slight curvatures. A more enhanced trabecular structure, composed of a network of shorter and thinner interconnected rods and plates, was seen toward the periphery of the metaphyseal region in both mice strains (Fig. 1). While the trabecular structures for both strains were similar, C3H bone had less that twice number of trabecula. We obtained this estimate from SEM images in Fig. 1 by counting both rod-like and plate-like trabeculae.

In the L5 vertebra, the SEM micrographs showed a well-defined trabecular bone structure, consisting of plate-like and rod-like trabeculae in both mice strains. The L5 vertebrae in the B6 mice (Fig. 2a) exhibited a clear reduction in bone volume and thinner, rod-like trabeculae compared to the thicker trabeculae and denser trabecular structure in C3H mice (Fig. 2b). Thus, the vertebral trabeculae of two mice strains differed in thickness and volume in contrast to femoral trabeculae, which showed less notable differences.

Microstructure

TEM images showed plywood type motifs in bone lamellar structure in both mouse strains. They exhibited the characteristic arcing patterns of the twisted plywood [31] or rotated plywood [32] arrangements as illustrated in Fig. 3a for B6 mouse bone and in Fig. 3b for C3H mouse bone. A transition consisting of oblique and cross-sectioned (transversely sectioned) fibrils was seen between the parallel layers of longitudinally sectioned fibrils in both mice strains. The transversely sectioned fibrils, however, were more distinguishable in the center of this transition region (Fig. 3). The successive layers of alternating longitudinally and transversely sectioned, demineralized fibrils, character-

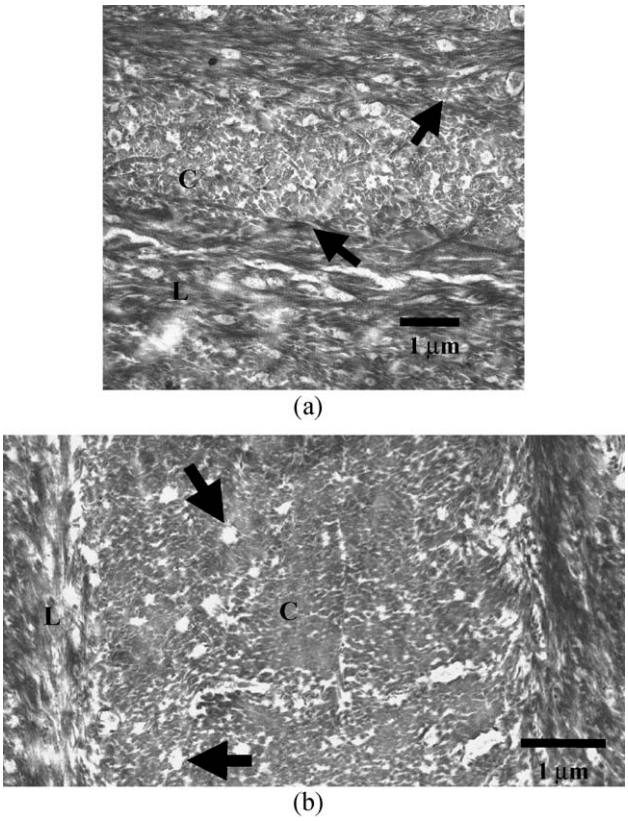

Fig. 4. TEM micrograph of alternating longitudinal (L) and transversely (C) sectioned demineralized fibrils from (a) B6 mouse and (b) C3H mouse. This is characteristic of the orthogonal plywood motif. Canaliculi (arrows), which appear as white elliptical bodies with variable length and size, are positioned in or traversing the lamellar structure.

istic of the orthogonal plywood motif, were also evident in both mice strains as seen in Figs. 4a and 4b for B6 and C3H mouse bone, respectively.

In Figs. 3 and 4, canaliculi, which appeared as white, elliptical bodies with variable length and size, were positioned in or traversing the lamellar structure. Analysis of the osteocyte network showed that canaliculi were ubiquitous throughout the lamellar structure in every C3H and B6 mouse bone micrograph. The osteocytes placement within the lamellar structure appeared to be equivalent between the two mice strains. In both mice types, the canaliculi were aligned roughly perpendicular to the lamellar boundary planes, and, in instances, were generally parallel to adjacent canaliculi or appeared as large, white, circular holes (Figs. 3 and 4). It was not possible to determine from the TEM micrographs if this vast canaliculi network altered the three-dimensional lamellar structure of either mouse strain.

Not all of the lamellar structures in the TEM micrographs of the B6 and C3H mouse bone correlated well with the plywood motifs. For instance, distinct differences were seen in the lamellar structures in Figs. 5 and 6, as compared to Figs. 3 and 4. In Figs. 5 and 6, the collagen arrangements did not follow classical plywood motifs in both mice strains. In Fig. 6, the characteristic banding pattern was replaced with regions consisting of oblique and cross-sectioned fibrils. Short, thin arrays of longitudinally sectioned fibrils, as well as white circular domains, reminiscent of canaliculi, broke up these oblique and transversely sectioned fibrils. A complete reversal of the arcing patterns (shown by dotted lines in Fig. 6) was observed between top and bottom portions of the micrograph. We found no distinct differences in these nonclassical patterns between two mice strains from the TEM images studied. These nonclassical banding patterns appear to occur near the osteocyte, suggesting that the collagen maybe nascent and still organizing in those locations.

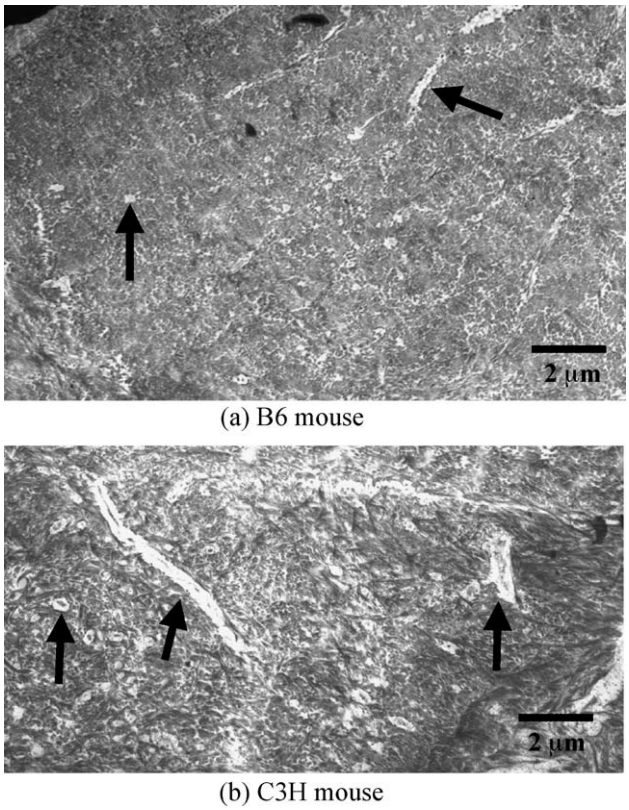

Fig. 5. TEM micrograph of demineralized bone from (a) B6 mouse and (b) C3H mouse, consisting of oblique and cross-sectioned fibrils showing no distinct collagen organization. Canaliculi (arrows) are seen with the oblique and transverse-sectioned fibrils.

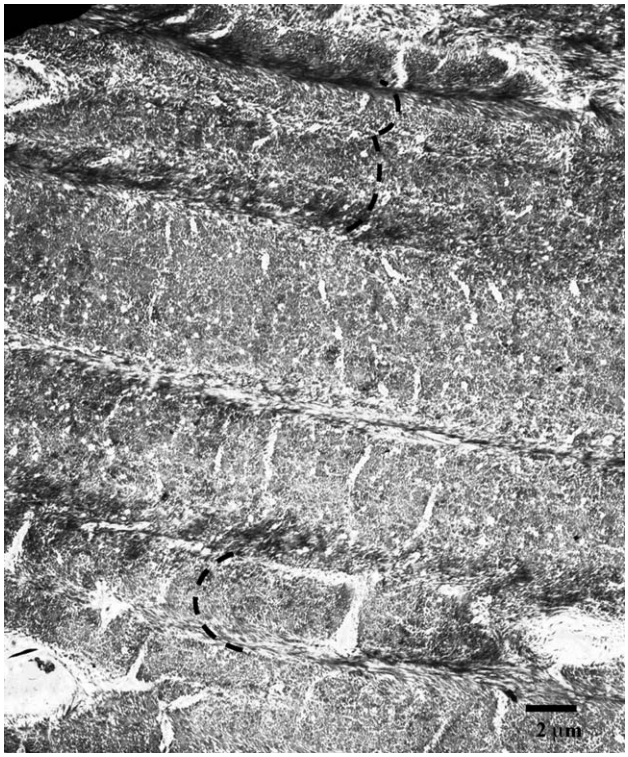

Fig. 6. TEM micrograph of demineralized lamellar structures from a C3H mouse showing a complete reversal of the arcing pattern (dotted lines) at the bottom and at the top portion of the image.

Nanostructure

At high magnifications of TEM, we were able to observe crystals and collagen fibrils at the nanostructural level in C3H and B6 mice bone, as illustrated in Figs. 7a and 7b, respectively. We found no apparent differences in the crystal-collagen structure between C3H and B6 mice. In Fig. 7a, the images of C3H mouse bone showed sharper contrasts and spatial variations in crystal density while in Fig. 7b the images of B6 mouse bone had a more uniform distribution of crystals. However, other images (not shown) of the nanostructural level exhibited such two behaviors in both mice strains. Both plate-like and tablet-like crystals were distinguished in C3H and B6 mice bone. The tablet-like crystals are actually plate-like crystals viewed on edge

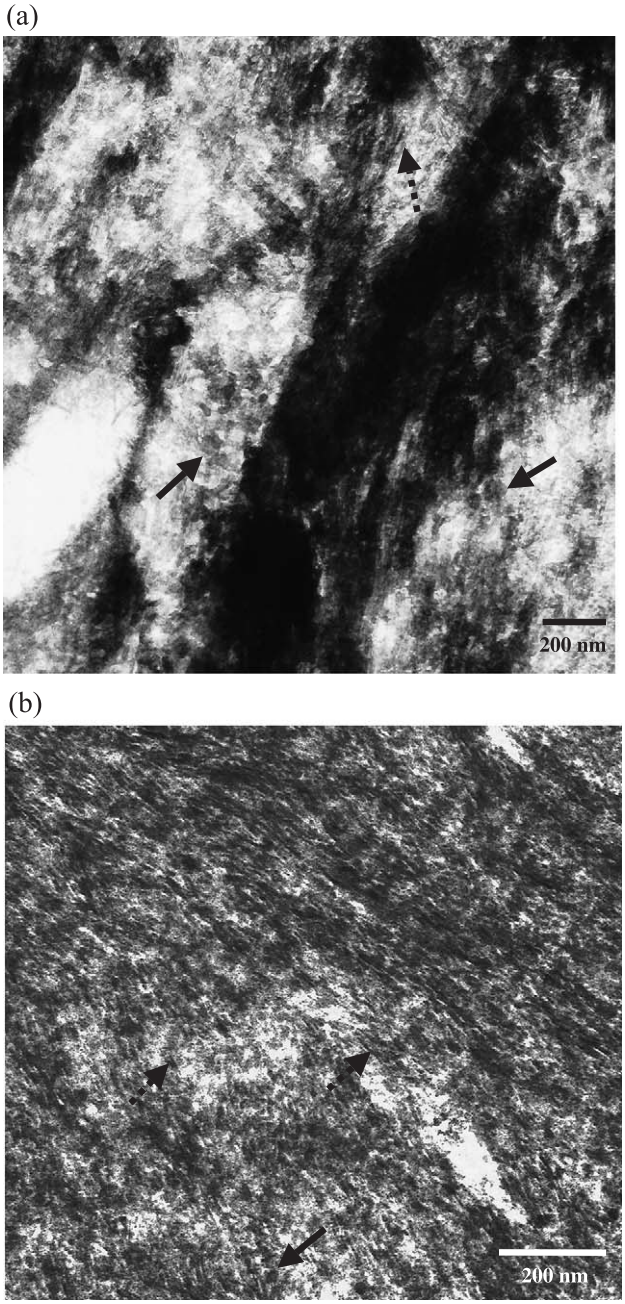

Fig. 7. TEM micrographs of C3H (a) and B6 (b) mouse trabecular bone showing distinct individual apatite crystals within the mineralized collagen fibrils as plate-like (arrows) and tablet-like shapes (plates on edge) (dotted arrows). The crystallographic *c*-axis of the crystals is generally aligned parallel to the long axis of the fibril.

(see Fig. 3 in Rubin et al. [33] for a sketch illustrating this point). There was also no significant difference in crystal size and morphology of the tablet-like crystals between C3H and B6 mice. The crystallographic *c*-axis of the plate-like and tablet-like crystals in both mice strains was generally aligned parallel to the long axis of the fibril. Crystal profiles of plate-like and tablet-like shapes were seen in the mineral region of C3H and B6 mouse bone in TEM images. However, the denseness of the bone matrix, as well as the crystal outline's merging and overlapping with one another, made it difficult to isolate individual crystals in C3H and B6 mice. The plate-like crystals' irregular shape and lighter appearance made them less detectable than the denser, tablet-like crystals. This made obtaining measurements for plate-like crystals nearly impossible. Due to the cluttering of the crystal profiles, it was also not possible to measure the length of the tablet-like crystals. However, the thickness of the crystals was readily seen and rather uniform throughout the micrographs. The average thickness of the crystals in C3H and B6 mice was 4.0 ± 0.4 and 4.2 ± 0.7 nm, respectively.

In summary, at the nanostructural level, we were able to make the following measurements and observations using the TEM images. We measured the crystal thickness (but not length or width), and we noted the shape of crystals (plate-like, as opposed to needle-like), the crystal orientation with respect to collagen fibrils, and the crystals alignment with the *c*-axis of the fibrils for both mice strains. We found no differences between C3H and B6 mice at this hierarchical level in these parameters.

Discussion

In the analysis of the hierarchical structure of C3H and B6 mice femoral and vertebral bone, presented in this paper, we have shown that the mesostructure is responsible for the differences in bone mineral density. Trabecular number, their density, and shapes vary at the two sites in the high- and low-density mouse models. Comparison of the microstructure and nanostructure of trabecular bone of these two mice strains, performed here for the first time, reveals no structural differences at these two lower scales. A more detailed discussion of the results is presented below.

Mesostructure

The histomorphometric analysis of Akhter et al. [25] and Amblard et al. [26] revealed that cancellous bone volume and thickness of trabeculae in metaphyseal of the femur were higher in C3H mice than in B6 mice. They also reported a greater trabecular number, which resulted in smaller trabecular spacing in C3H mice as compared with B6 mice. We confirmed qualitatively, by comparing SEM images from two mice strains, the results of Akhter et al. [25] and Amblard et al. [26] that there was a larger number of trabecula and smaller trabecular spacing in femoral metaphysis of C3H mice. In addition, our SEM micrographs revealed sparse trabecular structure in central metaphyseal regions of the femur becoming more enhanced toward the periphery of the metaphyseal region in both mice strains. Overall, the trabecular structure for the femorae of both mice strains had similar features when studied using SEM. In summary, our SEM observations of femorae confirm and complement histomorphometry results [25,26].

In the L5 vertebra, our SEM micrographs showed a well-defined and comparable trabecular structure, consisting of plate-like and rod-like trabeculae, in both mice strains. However, the B6 mice had a reduction in bone volume and thinner, rod-like trabeculae compared to the thicker trabeculae and denser trabeculae in C3H mice. These observations are in contrast with the results obtained by Turner et al. [10,11] by μCT, who reported a lack of three-dimensional trabecular bone structure in the L5 vertebrae of C3H mice compared to B6 mice. The mice used in Turner et al. were 16 weeks old, thus of the same age as mice used in our study. Thus, the reason for this discrepancy may be due to different experimental techniques used. SEM micrographs show bone structure but they give a two-dimensional image of vertebra trabecular structure. This allows qualitative analysis of mesostructure. To obtain stereographic measurements, three-dimensional information on structure is required but such data are not available from SEM. On the other hand, the μCT, which employs X-ray technology to identify hard tissue, captures a three-dimensional structure. This technique gives quantitative information on structure but it is sensitive to the resolution and the chosen threshold. In conclusion, our SEM results of vertebra trabecular structure, which do explain the higher bone mineral density in the vertebrae of the C3H mice, are in contrast with the previously published results of Turner et al. [10,11].

Microstructure

Collagen fibrils in C3H and B6 mice strains, seen in our TEM micrographs, had similar lamellar structures and were arranged in twisted, rotated, or orthogonal plywood motifs [31,32], which are characteristic of human and animal bone. However, not all of the lamellar structures in the TEM micrographs followed plywood models, and regions having no distinct collagen organization were also seen, suggesting that the lamellar structure of bone is more complicated than envisioned. There were no differences in bone structure in C3H and B6 mice trabecular bone at this level. Thus, we conclude that genetic differences between C3H and B6 mice strains do not influence bone structure at lamellar (microstructural) level.

Nanostructure

Although studies have shown that C3H mice have higher volumetric bone mineral density than B6 mice [11,13,24], we found no apparent differences in the crystal-collagen structure between C3H and B6 mice. Both plate-like and tablet-like crystals were distinguished in each mice strain, with tablet-like crystals being plate-like crystals viewed on edge [33]. The average thicknesses of the crystals in C3H and B6 mice were very similar and they measured about 4 nm. These results were consistent with the studies on bone crystal size [34,35]. The observed differences in local mineral density distributions in Fig. 7 are attributed to different stages of mineralization, distinct locations in lamellar structure, and to a lesser extent to different magnifications of shown images.

Our observation that crystals are thin platelets with irregular edges supports the results of the studies on crystal shape in mineralized tissue [32,34–36]. The results of our study are in disagreement, however, with the results obtained by Fratzl et al. [37], who characterized mouse bone crystals as being needle-like. In summary, our results suggest that the trabecular geometry, that is, the mesostructure, is responsible for differences in bone quality.

As discussed in the next section, we found strong similarities between the C3H and B6 mice bone and the normal and osteoporotic human bone structures. At the nanostructural level, we found no distinct differences in crystal size, shape, or their arrangement with respect to collagen fibrils between normal and osteoporotic bone [33]. Researchers disagree on the differences in crystal geometry in normal and osteoporotic bone. Our observations in Ref. [33] agree with those of Simmons et al. [38] that osteoporotic crystals are of the same size as the ones in normal bone. Other researchers report that osteoporotic crystals are either smaller [39] or larger [40,41] than those in normal bone. These differences may be attributed to different techniques used and difficulties in measurements due to very small crystal sizes [42]. The techniques used to measure crystal shape, size, and chemical composition include X-ray diffraction [38,43–45], Fourier transform-infrared (FTIR) technique [46–50], infrared spectrophotometry [51], small angle X-ray scattering (SAXS) [37,52–54], back scattering electron imaging (BSEI), Phosphorus-31 solid state nuclear magnetic resonance (NMR) [55,56], X-ray pole analysis [57,58], scanning electron microscopy (SEM), transmission electron microscopy (TEM) [59,60], and atomic force microscopy [61]. They all require processing of tissue and, thus, each technique is a subject to some limitations. A more complete discussion is given by us in Ref. [33]; see also Eppell et al. [61]. Thus, our TEM study provides information on crystal size and shape but using this technique we cannot assess crystal chemistry or crystallinity. Our conclusions are based on this limitation.

Comparison with normal and osteoporotic human bone

Our previous TEM study of human trabecular bone [33] shows nearly indistinguishable features at the meso-, micro-, and nanostructural levels to that of the murine bone studied here. Human osteoporotic bone differs from normal bone at the mesostructural level as represented by thinner or missing trabeculae, which results in increased porosity [38–40]. Indeed, the only structural level that differed between normal and osteoporotic human bone was the mesostructural level, where there was substantially less trabecular structure. This decline in mesostructure in human osteoporotic bone is comparable to the decreased trabecular structure seen in the B6 as compared with the C3H bone. In

essence, the major structural difference between C3H and B6 mouse bone represents either a deficiency in trabecular structure or a variation in trabeculae thickness. It is the combination of these two effects which makes up the differences in normal and osteoporotic human bone [62–64]. Thus, genetic differences between the two mouse strains may inform as to pathophysiological processes underlying osteoporosis.

In summary, SEM and TEM analyses of C3H and B6 mice showed significant structural variations only at the mesostructural level and not at the microstructural or nanostructural levels. Thus, the differences in bone mass affected the quality and constitution of bone only at the trabecular (mesostructural) level in C3H and B6 mice. This may indicate that the genetic makeup of the lamellar structure at the microstructural and nanostructural levels in the vertebrae and femur is independent of the amount of volumetric bone mineral density. The information on the hierarchical structure of bone should serve as valuable input in structure-property investigations of bone. The obtained results are subject to the limitations of techniques used. The SEM and TEM images provide only the information on bone structure and not on bone chemistry or its properties. Secondly, they only give a two-dimensional information on bone structure from which a partial three-dimensional data are inferred.

Acknowledgments

I.J. and J.R. acknowledge the support of the Emory/Georgia Tech Seed Grant Program 1999-2000 and I.J. acknowledges the support of the National Science Foundation (Grant CMS-0085137). The SEM and TEM work was conducted in the Integrated Microscopy and Microanalytical Facility at Emory University (Dr. Robert Apkarian, director). The authors would like to thank Dr. R. Apkarian and J. Taylor, the technologist, for their assistance in preparation and viewing of samples, and Mr. Andrew Yoo for his help in dissecting samples.

References

[1] Hui SL, Slemmenda CW, Johnston CC. Age and bone mass as predictors of fracture in a prospective study. J Clin Invest 1988; 81:1804–9.

[2] Eisman JA, Kelly PJ, Morrison NA, Pocock NA, Yeoman R, Birmingham J, et al. Peak bone mass and osteoporosis prevention. Osteoporos Int 1993;3(Suppl. 1):56–60.

[3] Smith DM, Nance WE, Kang KW, Christian JC, Johnston CC. Genetic factors in determining bone mass. J Clin Invest 1973;52: 2800–8.

[4] Pocock NA, Eisman JA, Hopper JL, Yeates MG, Sambrook PN, Ebert S. Genetic determinants of bone mass in adults. J Clin Invest 1987; 80:706–10.

[5] Pocock NA, Eisman JA, Hopper JL, Yeates MG, Sambrook PN, Ebert S. Genetic determinants of bone mass in adults: a twin study. J Clin Invest 1991;52:2800–8.

[6] Evans RA, Marel GM, Lancster EK, Kos S, Evans M, Wong YP. Bone mass is low in relatives of osteoporotic patients. Ann Intern Med 1988;109:870–3.

[7] Christian JC, Yu PL, Slemenda CW, Johnston CC. Heritability of bone mass: a longitudinal study in aging male twins. Am J Human Genet 1989;44:429–33.

[8] Slemenda CW, Christian JC, Williams CJ, Norton JA, Johnston Jr CC. Genetic determinants of bone mass in adult women: a reevaluation of the twin model and potential importance of gene interaction on heritability estimates. J Bone Miner Res 1991;6:561–7.

[9] Sheng M, Baylink D, Beamer W, Donahue L, Rosen C, Lau K, et al. Histomorphometric studies show that bone formation and bone mineral apposition rates are greater in C3H/HeJ (high-density) than C57BL/6J (low-density) mice during growth. Bone 1999;25(4): 421–9.

[10] Turner C, Hsieh YF, Muller R, Bouxsein M, Baylink D, Rosen C, et al. Genetic regulation of cortical and trabecular bone strength and microstructure in inbred strains of mice. J Bone Miner Res 2000;15(6):1126–31.

[11] Turner C, Hsieh YF, Muller R, Bouxsein M, Rosen C, McMcrann M, et al. Variation in bone biomechanical properties, microstructure, and density in BXH recombinant inbred mice. J Bone Miner Res 2001; 16(2):206–13.

[12] Akhter M, Cullen D, Pedersen E, Kimmel D, Recker R. Bone response to in vivo mechanical loading in two breeds of mice. Calcif Tissue Int 1998;63:442–9.

[13] Beamer WG, Donahue L, Rosen C, Baylink D. Genetic variability in adult bone density among inbred strains of mice. Bone 1996;18: 397–403.

[14] Chen C, Kalu N. Strain differences in bone density and calcium metabolism between C3H/HeJ and C57BL/6J mice. Bone 1999; 25(4):413–20.

[15] Dimai HP, Linkhart TA, Linkhart SG, Donahue LR, Beamer WG, Rosen CJ, et al. Alkaline phosphatase levels and osteoprogenitor cell numbers suggest bone formation may contribute to peak bone density differences between two inbred strains of mice. Bone 1998;22: 211–6.

[16] Kodama Y, Dimai HP, Wergedal J, Sheng M, Malpe, Kutilek S, et al. Cortical tibial bone volume in two strains of mice: effects of sciatic neurectomy and genetic regulation of bone response to mechanical loading. Bone 1999;25:183–90.

[17] Kodama Y, Miyakoshi N, Linkhart TA, Wergedal J, Srivastava A, Beamer W, et al. Effects of dietary calcium depletion and repletion on dynamic determinants of tibial bone volume in two inbred strains of mice. Bone 2000;27:445–52.

[18] Kodama Y, Umemura Y, Nagasawa S, Beamer W, Donahue L, Rosen C, et al. Exercise and mechanical loading increase periosteal bone formation and whole bone strength in C57BL/6J Mice but not in C3H/Hej mice. Calcif Tissue Int 2000;66:298–306.

[19] Li X, Srivastava AK, Gu W, Masinde G, Mohan S, Baylink DJ. Opposing changes in osteocalcin levels in bone vs. serum during at the acquisition of peak bone density in C3H/HeJ and C57BL/6J mice. Calcif Tissue Int 2002;71:416–20.

[20] Linkhart TA, Linkhart SG, Kodama Y, Farley JR, Dimai HP, Wright KR, et al. Osteoclast formation in bone marrow cultures from two inbred strains of mice with different bone densities. J Bone Miner Res 1999;14:39–46.

[21] Richman C, Kutilek S, Miyakoshi N, Srivastava AK, Beamer WG, Donahue LR, et al. Postnatal and pubertal skeletal changes contribute predominately to the differences in peak bone density between C3H/Hej and C57BL/6J Mice. J Bone Miner Res 2001;16(2): 386–97.

[22] Rosen CJ, Churchill GA, Donahue LR, Shultz KL, Burgess JK, Powell DR, et al. Mapping quantitative trait loci for serum insulin-like growth factor-1 levels in mice. Bone 2000;27:521–8.

[23] Rosen CJ, Dimai HP, Vereault D, Donahue LR, Beamer WG, Farley J, et al. Circulating and skeletal insulin-like growth factor-I (IGF-I)

concentrations in two inbred strains of mice with differential bone mineral densities. Bone 1997;21:217–23.
[24] Beamer WG, Shultz KL, Churchill GA, Frankel WN, Baylink DJ, Rosen CJ, et al. Quantitative trait loci for bone density in C57BL/6J and CAST/EiJ inbred mice. Mamm Genome 1999;10:1043–9.
[25] Akhter M, Iwaniec U, Cullen D, Kimmel D, Recker R. Genetic variations in bone density, histomorphometry, and strength in mice. Calcif Tissue Int 2000;67:337–44.
[26] Amblard D, Lafage-Proust M-H, Laib A, Thomas T, Ruegsegger P, Alexandre C, et al. Tail suspension induces bone loss in skeletally mature mice in the C57BL/6J strain but not in the C3H/HeJ strain. J Bone Miner Res 2003;18:561–9.
[27] Jayasinghe J, Jones SJ, Boyde A. Scanning electron microscopy of human lumbar vertebral trabecular bone surfaces. Virchows Arch, A Pathol Anat 1993;422:25–34.
[28] Mosekilde L. Consequences of the remodeling process for vertebral trabecular bone-structure—A scanning electron-microscopy study (uncoupling of unloaded structures). Bone Miner 1990;10:13–35.
[29] Traub W, Arad T, Weiner S. Three-dimensional ordered distribution of crystals in turkey in tendon collagen fibers. Proc Natl Acad Sci U S A 1989;86:9822–6.
[30] Weiner S, Arad T, Sabanay I, Traub W. Rotated plywood structure of primary lamellar bone in the rat: orientations of the collagen fibril arrays. Bone 1997;20(6):509–14.
[31] Giraud-Guille MM. Twisted plywood architecture of collagen fibrils in human compact bone osteons. Calcif Tissue Int 1988;42:167–80.
[32] Weiner S, Price P. Disaggregation of bone into crystals. Calcif Tissue Int 1986;39:365–75.
[33] Rubin MA, Jasiuk I, Taylor J, Rubin J, Ganey T, Apkarian R. TEM analysis of the nanostructure of normal and osteoporotic human trabecular bone. Bone 2003;33:270–82.
[34] Robinson R. An electron microscopic study of the crystalline inorganic component of bone and its relationship to the organic matrix. J Bone Joint Surg 1952;34:389–435.
[35] Jackson SA, Cartwright LD, Lewis D. The morphology of bone mineral crystals. Calcif Tissue Res 1978;25:217–22.
[36] Landis WJ, Song M. Mineral and organic matrix interaction in normally calcifying tendon visualized in three dimensions by high voltage electron microscopic tomography and graphic image reconstruction. J Struct Biol 1993;110:39–54.
[37] Fratzl P, Groschner M, Vogl G, Plenk H, Eschberger J, Fratzl-Zelman N, et al. Mineral crystals in calcified tissues: a comparative study by SAXS. J Bone Miner Res 1992;7:329–34.
[38] Simmons Jr ED, Pritzker KPH, Grynpas MD. Age-related changes in human femoral cortex. J Orthop Res 1991;9:155–67.
[39] Grynpas MD, Holmyard D. Changes in quality of bone mineral on aging and in disease. Scanning Microsc 1988;2:1045–54.
[40] Baud CA, Pouezat J, Tochon-Danguuy H. Quantitative analysis of amorphous and crystalline bone tissue mineral in women with osteoporosis. Calcif Tissue Int 1976;21S:452–6.
[41] Chatterji S, Wall JC, Jefferey JW. Age related changes in the orientation and particle size of the mineral phase in human cortical bone. Calcif Tissue Int 1981;33:567–74.
[42] Boskey AL. Bone mineral and matrix: are they altered in osteoporosis? Orthop Clin North Am 1990;21:19–29.
[43] Ampino E, Engstron A. Studies on X-ray absorption and diffraction of bone tissues. Acta Anat 1952;15:1–22.
[44] Bonar LC, Roufosse AH, Sabine WK, Grynpas MD, Glimcher MJ. X-ray diffraction studies of the crystallinity of bone mineral in newly synthesized and density fractioned bone. Calcif Tissue Int 1983;35:202–9.
[45] Grynpas MD, Bonar LC, Glimcher MJ. X-ray diffraction radial distribution function studies on bone mineral and synthetic calcium phosphates. J Mater Sci 1984;19:723–36.
[46] Boskey AL, Gadaleta S, Gundberg C, Doty SB, Ducy P, Karsenty G. Fourier transform infrared microspectroscopic analysis of bones of osteocalcin-deficient mice provides insight into function of osteocalcin. Bone 1997;23:187–96.
[47] Camacho NP, Rinnerthaler S, Paschalis EP, Mendelsohn R, Boskey AL, Fratzl P. Complementary information on bone ultrastructure from scanning small angle X-ray scattering and Fourier-transform infrared microspectroscopy. Bone 1999;25:287–93.
[48] Paschalis EP, Betts F, DiCarlo E, Mendelsohn R, Boskey AL. FTIR microspectroscopic analysis of normal human cortical and trabecular bone. Calcif Tissue Int 1997;61:480–6.
[49] Paschalis EP, Betts F, DiCarlo E, Mendelsohn R, Boskey AL. FTIR microspectroscopic analysis of human iliac crest biopsies from untreated osteoporotic bone. Calcif Tissue Int 1997;61:487–92.
[50] Paschalis EP, DiCarlo E, Betts F, Sherman P, Mendelsohn R, Boskey AL. FTIR microspectroscopic analysis of human osteonal bone. Calcif Tissue Int 1996;59:480–7.
[51] Cohen L, Kitzes R. Infrared spectroscopy and magnesium content of bone mineral in osteoporotic women. Isr J Med Sci 1981;17:1123–5.
[52] Fratzl P, Roschger R, Eschberger J, Abendroth B, Klaushofer K. Abnormal bone mineralization after fluoride treatment in osteoporosis: a small-angle X-ray scattering study. J Bone Miner Res 1994;9(10):1541–9.
[53] Fratzl P, Schreiber S, Boyde A. Characterization of bone mineral crystals in horse radius by small-angle X-ray scattering. Calcif Tissue Int 1996;58:341–6.
[54] Fratzl P, Fratzl-Zelman N, Klaushofer K, Vogl G, Koller K. Nucleation and growth of mineral crystals in bone studied by SAXS. Calcif Tissue Int 1991;48:407–13.
[55] Bohic S, Rey C, Legrand A, Sfihi H, Rohanizadeh R, Martel C, et al. Characterization of the trabecular rat bone mineral: effect of ovariectomy and bisphosphonate treatment. Bone 2000;26(4):341–8.
[56] Wu Y, Ackerman JL, Kim H-M, Rey C, Barroug A, Glimcher MJ. Nuclear magnetic resonance spin-spin relaxation of the crystals of bone, dental enamel, and synthetic hydroxyapatites. J Bone Miner Res 2002;17:472–80.
[57] Nightingale JP, Lewis D. Pole figures of the orientation of apatite in bones. Nature 232:334–335.
[58] Sasaki N, Sudoh Y. X-ray pole figure analysis of apatite crystals and collagen molecules in bone. Calcif Tissue Int 1997;60:361–7.
[59] Prostak KS, Lees S. Visualization of crystal matrix structure. In situ demineralization of mineralized turkey tendon and bone. Calcif Tissue Int 1996;59:474–9.
[60] Landis W, Hodgens K, Arena J, Song M, McEwen B. Structural relations between collagen and mineral in bone as determined by high voltage electron microscopic tomography. Microsc Res Tech 1996;33:192–202.
[61] Eppell SJ, Tong W, Katz JL, Kuhn L, Glimcher MJ. Shape and size of isolated bone mineralites measured using atomic force microscopy. J Orthop Res 2001;19:1027–34.
[62] Reid SA. Micromorphological characterization of normal human bone surfaces as a function of age. Scanning Microsc 1987;1(2):579–97.
[63] Schnitzler CM. Histomorphology of osteoporosis. In: An YH, editor. Orthopaedic Issues in Osteoporosis. Boca Raton (FL): CRC Press; 2003. p. 19–37.
[64] Consensus Development Conference: prophylaxis and treatment of osteoporosis. Am J Med 1991;90:107.